# BRAGG REFLECTION IN OPTICAL WAVEGUIDES

Thesis by

George X. Ouyang

In Partial Fulfillment of the Requirements for the

Engineer's Degree

CALIFORNIA INSTITUTE OF TECHNOLOGY

Pasadena, California

2004

(Defended May 10, 2004)

To My Parents

© 2004

George X. Ouyang

# ACKNOWLEDGEMENTS

This thesis would not have been possible without the guidance, friendship and assistance of numerous people. I'd like to thank my research adviser, Professor Amnon Yariv, for his continuous guidance and support, and the rest of my research group: Yong Xu, Reginald Lee, Wei Liang, Koby Scheuer, George Paloczi, Will Green, John Choi, Shervin Taghavi, Joyce Poon, Yanyi Huang and Lin Zhu for many valuable suggestions and interesting discussions.

I'm also grateful to all the friends I've made throughout my years at Caltech, including but not limited to: Song Wang, Yanbei Chen, Xinkai Wu, and Guodong Wang. They have made my life at Caltech both educational and enjoyable.

# ABSTRACT

In this dissertation I explore the phenomenon of Bragg reflection in optical waveguides. Two specific waveguide structures are studied in detail: the Bragg fiber and a generic planar waveguide with a Bragg grating etched in it.

Bragg fibers can be classified into two groups: the air-core Bragg fiber and the coaxial Bragg fiber. Whereas the former has a plain air core at the center, the latter contains an additional high-index column in the core. Using a perturbative approach I study and compare the dispersion properties of the two types of fibers, with special attention to their potential for truly single-mode transmission. As the result a large single-mode frequency window, which also includes a zero-dispersion point, is found for the TM mode in the coaxial fiber,

The air-core Bragg fiber is also studied as a potential candidate for dispersion compensation. It is found that Bragg reflections in the fiber are capable of producing negative dispersion values at least as large as -20,000 ps/(nm·km), which is a twenty-fold improvement over previous results. The fiber parameters used for this study are somewhat unrealistic however, and further improvement is necessary before a Bragg fiber can be deployed as a Dispersion Compensating Fiber (DCF).

Optical filters based on Bragg grating structures also involve Bragg reflections. While continuous Fiber Bragg Gratings (FBG's) have long been studied and deployed as practical reflection filters, the possibility of etching a discrete grating in a (planar) waveguide has to my knowledge, never been investigated. In this dissertation I propose a novel scheme for designing such a grating, which is implemented by discretizing its continuous counterpart into a series of air holes. The relationship between the two gratings (discrete and continuous) is established in terms of the grating strength and the local grating period.

TABLE OF CONTENTS

# LIST OF FIGURES

*Chapter 1*

# INTRODUCTION

The propagation of electromagnetic radiation in periodic media has been a subject of interest because of its wide ranging applications. The simplest example of a periodic medium consists of alternating layers of two different materials with different refractive indices. Wave propagating in these media exhibits many interesting and potentially useful phenomena. Among the most widely used is the phenomenon of Bragg reflection.

Bragg reflection, in the most general terms, is a multiple scattering process which, through careful placement of the scattering centers/planes, leads to high reflectance via constructive interference. The scattering centers/planes are usually periodically distributed, though sometimes a little perturbation in position could also be tolerated.

In this dissertation I would like to investigate how the same Bragg reflection process can be used differently in different applications. Specifically I would like to explore this phenomenon in two distinct structures: a Bragg fiber and a discrete grating in a planar waveguide. As will be shown in later chapters, Bragg reflections occur in the transverse direction in the Bragg fiber, whereas in the grating, they take place along the longitudinal direction.

The rest of the dissertation is organized as follows: in Chapter 2 I compare two types of Bragg fibers --- the air-core Bragg fiber and the coaxial Bragg fiber --- in hope of finding a frequency window for truly single-mode (TE or TM) transmission. In Chapter 3 I explore the potential of air-core Bragg fibers as group velocity dispersion compensators. Chapter 4 is dedicated to the discretization in a planar waveguide of continuous and nearly-uniform Bragg gratings.

*C h a p t e r   2*

BRAGG FIBERS: AIR-CORE VS COAXIAL

## 2.1 Introduction

In conventional optical fibers, light confinement is achieved through total internal reflection and photons propagate mainly in the high index center core. A completely different confinement mechanism, Bragg reflection, provides an alternative way of guiding photons. This possibility was first pointed out by Yeh et al. in [1], where the concept of Bragg fiber was first introduced.

Since Bragg fibers and conventional optical fibers utilize different guiding mechanisms, it is not surprising that Bragg fibers offer many possibilities that are difficult to achieve in conventional fibers. One such example is the possibility of guiding light in air, which has attracted much recent interest [2]-[6].

A Bragg fiber can also be designed to support a single guided mode without azimuthal dependence (i.e. the TE or the TM mode). In contrast with the fundamental mode in conventional fibers, which is always doubly degenerate, these guided Bragg fiber modes are truly single mode. Consequently, many undesirable polarization dependent effects can be completely eliminated in Bragg fibers [6].

One variant of the original Bragg fiber, which has a uniform low-index core, is the so-called coaxial Bragg fiber [6]. Coaxial Bragg fibers also guide light through Bragg reflection, except now that a smaller high-index column is embedded at the center of the low-index core. Fig. 1 gives a schematic comparison of the two fibers. For ease of comparison, I choose the same cladding structure for both waveguides: layer 1 has an index of refraction $n_1 = 4.6$ and a thickness $d_1 = 0.333a$, whereas layer 2 has an index of refraction $n_2 = 1.6$ and a thickness $d_2 = 0.667a$. Here, $a = d_1 + d_2$ is the period of the cladding

layers. The cores of the two fibers are different: whereas the Bragg fiber has only a uniform core with an index of refraction $n_o = 1.0$ (i.e. an air-core Bragg fiber) and a radius $r_o$, the coaxial fiber core contains an additional inner core with an index of refraction $n_i$ and a radius $r_i$. For simplicity I choose to vary only three parameters in my study: $n_i$, $r_i$, and $r_o$.
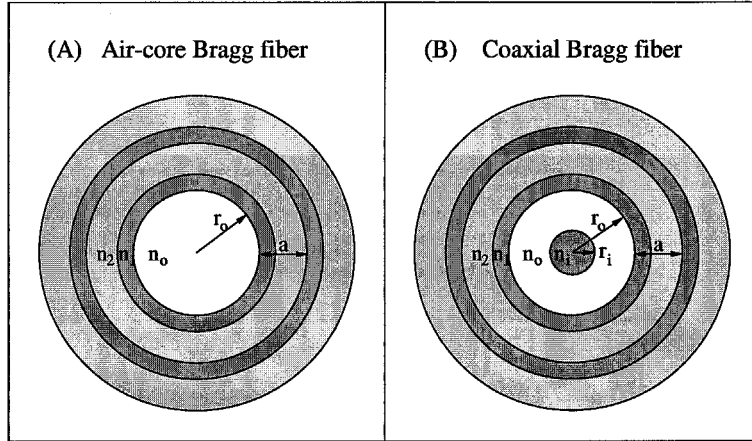


Fig. 1. Air-core and coaxial Bragg fiber cross sections. (A) Air-core Bragg waveguide, and (B) Coaxial Bragg waveguide. Cladding layer 1 has an index of refraction $n_1 = 4.6$ and a thickness $d_1 = 0.333a$ (not shown), whereas layer 2 an index of refraction $n_2 = 1.6$ and a thickness $d_2 = 0.667a$ (not shown), where $a = d1 + d2$ is the period of the cladding. The white region in the core is assumed to be filled with air, with an index of refraction $n_o = 1$. Three parameters are subject to change in this study: $n_i$, the index of the refraction of the inner core in (B); $r_i$, the radius of the inner core in (B); and $r_o$, the outer core radius in both (A) and (B). Note that an air-core Bragg fiber can be thought as a coaxial Bragg fiber with $r_i = 0$.

For the calculations presented here, I have also filled the coaxial waveguiding region (the white region in Fig. 1(B)) with air. In practice, in order to provide structural support it may be replaced by some dielectric material with a low index of refraction without greatly affecting the main observation. Many interesting features can potentially be introduced by the presence of a high index inner core, but in this dissertation I am mainly interested in its effect on the dispersion relation of the fiber and whether or not it can lead to a frequency window of single-mode transmission.

## 2.2 Theoretical Analysis

### 2.2.1 *Asymptotic Calculations*

In [7] Xu et al. developed a general matrix theory for cylindrically symmetric waveguides with Bragg claddings. In this theory, an arbitrary number of inner dielectric layers are treated exactly and the outside cladding layers are approximated in the asymptotic limit. Approximate mode equations are derived by matching the boundary conditions at the interface and dispersion relations can be found by numerically solving these mode equations. For more information about the asymptotic calculations, the reader is referred to [7].

Using the asymptotic formalism, one can find confined modes for both the Bragg and the coaxial fibers in the bandgap. With $n_i = 4.6$, $r_o = 1.4a$, and the cladding parameters given in Fig. 1, I plot the dispersion relations in Fig. 2 for a number of inner core radius $r_i$.
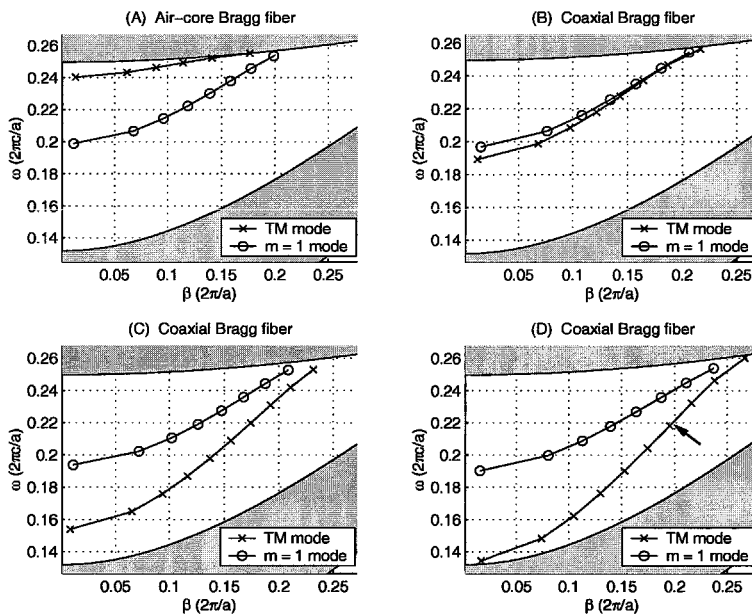


Fig. 2. Dispersion diagrams for $n_i = 4.6$ and $r_o = 1.4a$. $r_i$ is varied as follows: (A) $r_i = 0$ (air-core Bragg fiber), (B) $r_i = 0.133a$, (C) $r_i = 0.2a$, and (D) $r_i = 0.267a$. Note in (D) the TM mode exhibits single-mode behaviour in the lower half of the bandgap, which does not include the zero-dispersion point identified by the arrow.

The main observation here is that as the inner core radius $r_i$ is increased from $r_i = 0$ (air-core Bragg fiber) to $r_i = 0.267a$, the TM band undergoes a large downward shift in frequency whereas the $m = 1$ band moves very little, creating a large single-mode transmission window for the TM mode in the lower half of the bandgap.

Before I begin exploring the downward shifts of the dispersion bands, it is instructive to first take a look at the field profiles along the radial direction inside the two fibers. In Fig. 3 I plot the $\vec{E}$ field profiles for both the TM and the $m = 1$ modes and for later convenience I choose modes with the same propagation wavevector $\beta$. Note the drastic reduction in field amplitude for the $m = 1$ mode inside the inner core of the coaxial fiber (Compare Fig. 3(B) with Fig. 3(D)).
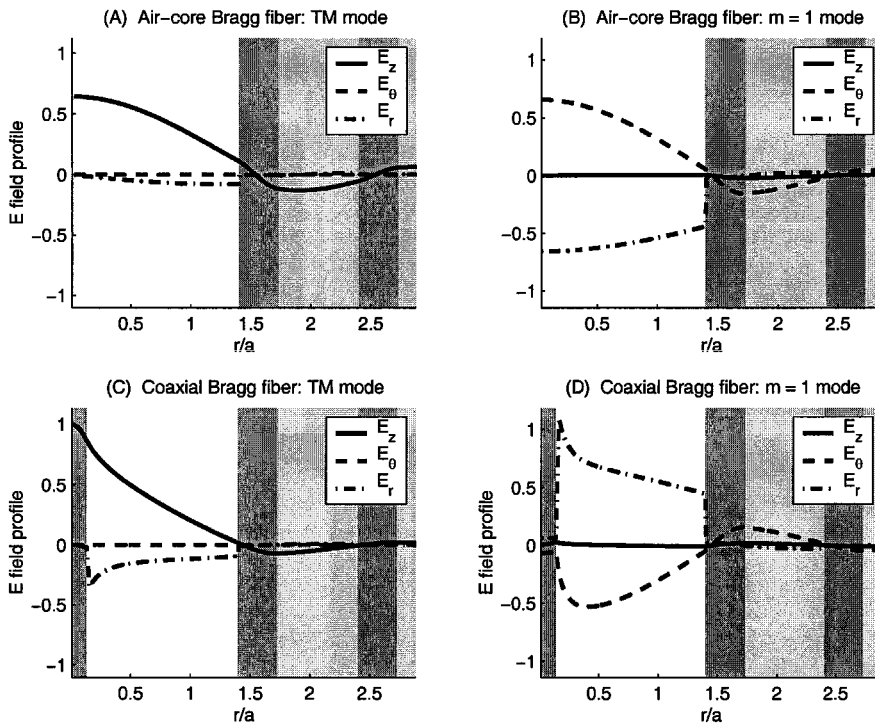


Fig. 3. $\vec{E}$ field profiles for $n_i = 4.6$ and $r_o = 1.4a$. The air-core Bragg fiber has a $r_i = 0$ whereas for the coaxial Bragg fiber $r_i = 0.133a$. The propagation constant $\beta = 0.05(2\pi/a)$ for all four modes and the eigen frequencies $\omega$ are found to be: (A) $\omega = 0.2430(2\pi c/a)$, (B) $\omega = 0.2040(2\pi c/a)$, (C) $\omega = 0.1943(2\pi c/a)$, (D) $\omega = 0.2018(2\pi c/a)$. Note in (D) the large jump discontinuity at the core boundary for $E_r$.

## 2.2.2 *Perturbation Analysis*

The disparate behaviours of the two bands under the influence of a high-index inner core can be explained by perturbation theory. Under the perturbation approach, one treats the inner core as a perturbation to an air-core Bragg fiber structure and solve the wave equation for correction to the unperturbed eigenmode frequency.

For a fixed propagation wavevector $\beta$, let the unperturbed modes of an air-core Bragg fiber be:

$$\vec{E}_m = \vec{\varepsilon}_m(r,\theta)\exp[i(\beta z - \omega_m t)], \qquad m = 0,1,2,...,$$

which satisfy the unperturbed eigenmode equation:

$$\nabla \times \nabla \times \vec{E}_m = \varepsilon(r,\theta)\left(\frac{\omega_m}{c}\right)^2 \vec{E}_m \qquad (2\text{-}1)$$

These modes form a complete orthogonal set and obey the orthonormal relation [8]:

$$\int d\vec{r}\,\varepsilon(\vec{r})\vec{F}_n^*(\vec{r}) \cdot \vec{F}_m(\vec{r}) = \delta_{m,n} \qquad (2\text{-}2)$$

Now consider the effect of a dielectric perturbation $\Delta\varepsilon(r,\theta)$ induced by the high-index inner core. Let $\delta\vec{E}_m$ and $\delta\omega_m$ be the changes in the mode functions and eigen frequencies, respectively. The eigenmode equation now takes the form:

$$\nabla \times \nabla \times (\vec{E}_m + \delta\vec{E}_m) = (\varepsilon + \Delta\varepsilon)\left(\frac{\omega_m + \delta\omega_m}{c}\right)^2 (\vec{E}_m + \delta\vec{E}_m) \qquad (2\text{-}3)$$

In a perturbation analysis, one normally neglects the second-order terms such as $\Delta\varepsilon\delta\vec{E}_m$ when expanding the right-hand side of (2-3). In this case, however, not all second-order terms are negligible. For example, as I noted earlier, the correction in mode function $\delta\vec{E}_m$

may be large in the inner core region of the coaxial fiber (Compare Fig. 3(B) with Fig. 3(D)). Also, the fractional change in $\varepsilon(r,\theta)$ may also be significant owing to the large index of refraction of the inner core (For $n_i = 4.6$, $\Delta\varepsilon = n_i^2 - 1 = 20.16 \gg 1.0$). So the only quantity here that can be made small is $\delta\omega_m$, provided the size of the inner core is small enough (See Fig. 2).

Assuming that the second-order term $(\delta\omega_m)^2$ can be neglected, one can expand (2-3) and then simplify by making use of (2-1):

$$\nabla \times \nabla \times (\delta\vec{E}_m) = \left(\frac{\omega_m}{c}\right)^2 \left[\varepsilon\delta\vec{E}_m + \Delta\varepsilon(\vec{E}_m + \delta\vec{E}_m)\right] + \left(\frac{2\omega_m}{c^2}\right)\delta\omega_m(\varepsilon + \Delta\varepsilon)(\vec{E}_m + \delta\vec{E}_m) \quad (2\text{-}4)$$

To solve this equation I expand $\delta\vec{E}_m$ in terms of the unperturbed mode functions:

$$\delta\vec{E}_m = \sum_n a_{mn}\vec{E}_n \quad (2\text{-}5)$$

where the $a_{mn}$'s are constants. Substituting (2-5) for $\delta\vec{E}_m$ in (2-4) and once again making use of (2-1), I get:

$$\sum_n a_{mn}\left[\left(\frac{\omega_n}{c}\right)^2 - \left(\frac{\omega_m}{c}\right)^2\right]\varepsilon\vec{E}_n = \left[\left(\frac{\omega_m}{c}\right)^2\Delta\varepsilon + \left(\frac{2\omega_m}{c^2}\right)\delta\omega_m(\varepsilon + \Delta\varepsilon)\right](\vec{E}_m + \delta\vec{E}_m) \quad (2\text{-}6)$$

Scalar multiplying both sides by $\vec{E}_m^*$ and integrating over all space, one finds that the expression on the left vanishes because of the orthogonal property (2-2), with the resulting equation being:

$$\int d\vec{r}\left(\frac{2\omega_m}{c^2}\right)\delta\omega_m(\varepsilon + \Delta\varepsilon)\vec{E}_m^* \cdot (\vec{E}_m + \delta\vec{E}_m) = -\int d\vec{r}\left(\frac{\omega_m}{c}\right)^2\Delta\varepsilon\vec{E}_m^* \cdot (\vec{E}_m + \delta\vec{E}_m) \quad (2\text{-}7)$$

Since $\delta\omega_m$ is a constant, it can be pulled outside the integral:

$$\delta\omega_m = -\left(\frac{\omega_m}{2}\right)\frac{\int d\vec{r}\,\Delta\varepsilon\vec{E}_m^* \cdot (\vec{E}_m + \delta\vec{E}_m)}{\int d\vec{r}(\varepsilon + \Delta\varepsilon)\vec{E}_m^* \cdot (\vec{E}_m + \delta\vec{E}_m)} \qquad (2\text{-}8)$$

The above expression can now be used to explain the different effects that a high-index inner core has on the TM and the $m = 1$ bands. First note that $\Delta\varepsilon$ is a windowing function that is nonzero only inside the inner core, hence for the mode function $(\vec{E}_m + \delta\vec{E}_m)$ in the top integral, only the portion that falls inside the inner core will contribute.

For the TM band, one notes from Fig. 3(C) that the TM mode has a large $E_z$ component inside the inner core, which would make a significant contribution to the top integral in (2-8). This explains why the TM band makes a large downward shift in frequency even with the insertion of a relatively small inner core. In the case of the $m = 1$ band, I refer back to Fig. 3(D), which shows a very small $\vec{E}$ field inside the inner core. Hence only a small $\delta\omega$ is to be expected, as verified by Fig. 2 where the $m = 1$ band moves very little for the given range of $r_i$'s.

But then why is it that the TM mode can have a large $\vec{E}$ field inside the inner core and the $m = 1$ mode can't? Appendix A provides us with a clue. For the TM mode, one realizes from Appendix A that it has two $\vec{E}$ field components in the inner core: $E_z$ and $E_r$, which are proportional to the zeroth order Bessel's function $J_0(k_{co}r)$ and first order Bessel's function $J_1(k_{co}r)$ respectively, where $k_{co}$ is the transverse wavevector inside the core. Assuming the core is small and knowing that $J_0(0) = 1$ and $J_1(0) = 0$, we see that $E_z$ would necessarily be large and $E_r$ would necessarily be small.

The situation is different for the $m = 1$ mode. From Appendix A, one finds that all three $\vec{E}$ field components, $E_z$, $E_r$, and $E_\theta$, are present in the inner core. The $E_z$ component can be neglected because it is proportional to $J_1(k_{co}r)$, whereas $E_r$ and $E_\theta$ each contains a

$J_0(k_{co}r)$ term and are equal in amplitude at $r = 0$. For a high-index core with $n_i = 4.6$ and an air region outside, boundary matching imposes a large jump discontinuity at the boundary for $E_r$. In fact, at the boundary $E_r^{air} = n_i^2 E_r^{core} = 21.16 E_r^{core}$. This explains why $E_r$ is necessarily small in a high-index center core after the mode function has been properly normalized. $E_\theta$ is also small in the core because it's been tied down with $E_r$ at $r = 0$, (i.e., $E_\theta(0) = E_r(0)$ in amplitude). As a final remark, we should note the same boundary conditions do not have the same "clamping" effect on the TM mode, where the predominant component is $E_z$, which is continuous across the core boundary.

To verify the validity of my perturbation analysis, I lower the index of refraction of the inner core and repeat the same asymptotic calculations that have produced Fig. 2. The resulting band diagrams for $n_i = 1.45$ and $r_o = 1.4a$ are plotted in Fig. 4, and the corresponding field profiles in Fig. 5.
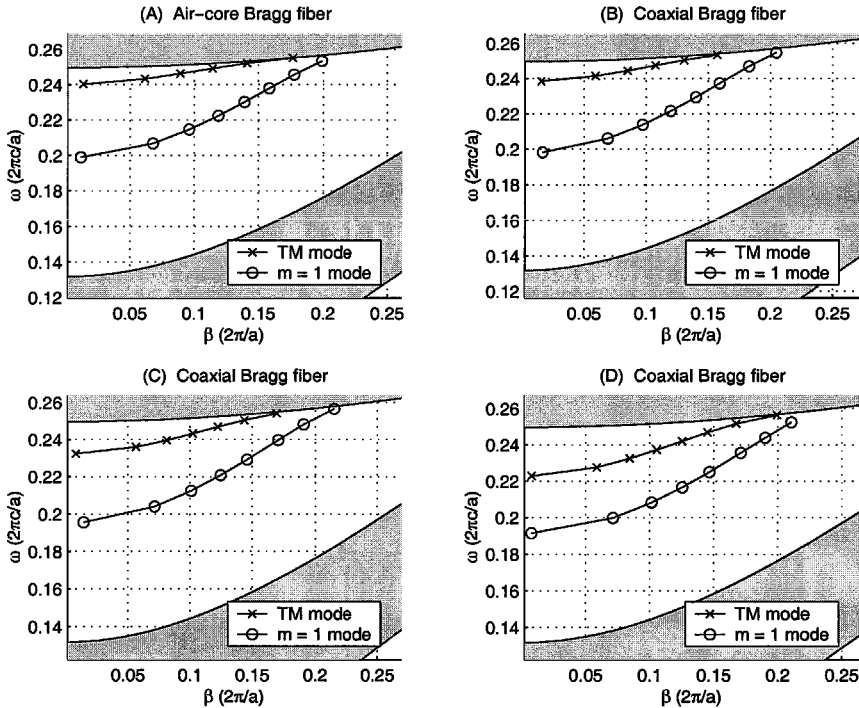


Fig. 4. Dispersion diagrams for $n_i = 1.45$ and $r_o = 1.4a$. $r_i$ is varied as follows: (A) $r_i = 0$ (air-core Bragg fiber), (B) $r_i = 0.133a$, (C) $r_i = 0.267a$, and (D) $r_i = 0.4a$. Note the downward shifts of the two bands are small compared to those of Fig. 2.
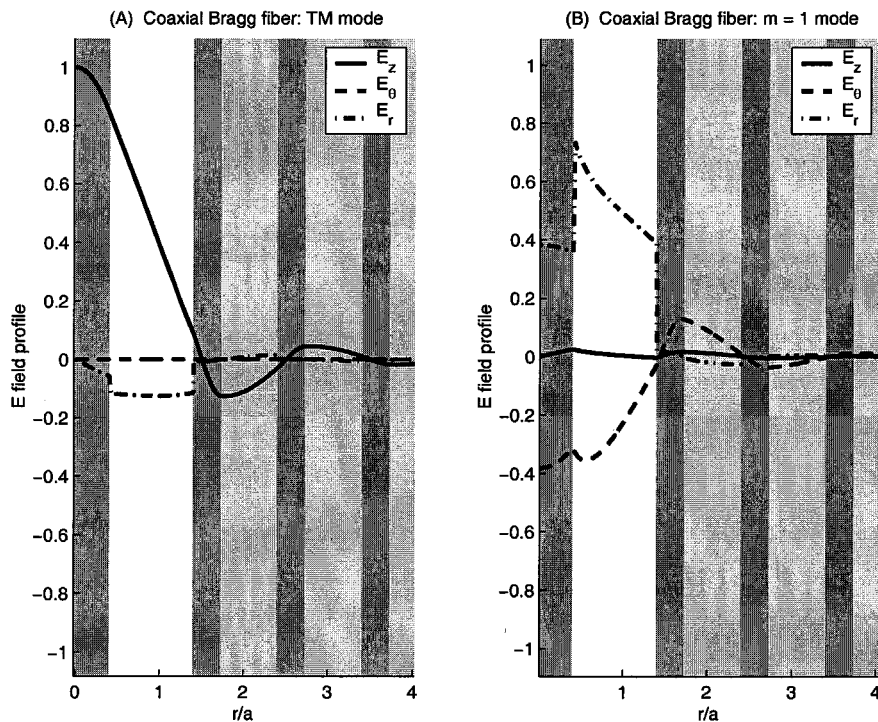
Fig. 5. $\vec{E}$ field profiles for $n_i = 1.45$, $r_i = 0.4a$, and $r_o = 1.4a$. The propagation constant $\beta = 0.05(2\pi/a)$ for both plots and the eigen frequency $\omega$ are found to be: (A) $\omega = 0.2267(2\pi c/a)$, (B) $\omega = 0.1966(2\pi c/a)$. Note that in (B) the jump discontinuity for $E_r$ at the core boundary is not as sharp as that of Fig. 3(D).

According to the above analysis, the clamping effect imposed by the boundary conditions on the $E_r$ component of the $m = 1$ mode should not be nearly as prominent as before owing to the greatly reduced index of refraction in the core. As a result, the downward shifts of the TM band and the $m = 1$ band should be much smaller than before and of the same order of magnitude. This is exactly what one observes in Fig. 4, although the downward shift of the TM band is still larger because the inner core still provides some clamping even with the reduced index of refraction.

Having found a single-mode transmission window for the TM band in Fig. 2(D), I now explore the possibility of including a zero-dispersion point in this window. If I reduce the outer core radius $r_o$ initially to push both the TM and the $m = 1$ bands higher up in the bandgap for the air-core Bragg fiber, then when the inner core is added, I know the $m = 1$

band will pretty much stay high up in the bandgap while the TM band will come down all the way to the bottom. In this way I can extend the single-mode frequency window and hopefully it will also include a zero-dispersion point. This is exactly what I did and the resulting band diagrams for $n_i = 4.6$ and $r_o = 0.867a$ are plotted in Fig. 6. Note the arrow that points to the zero-dispersion point inside the single-mode window in Fig. 6(D).
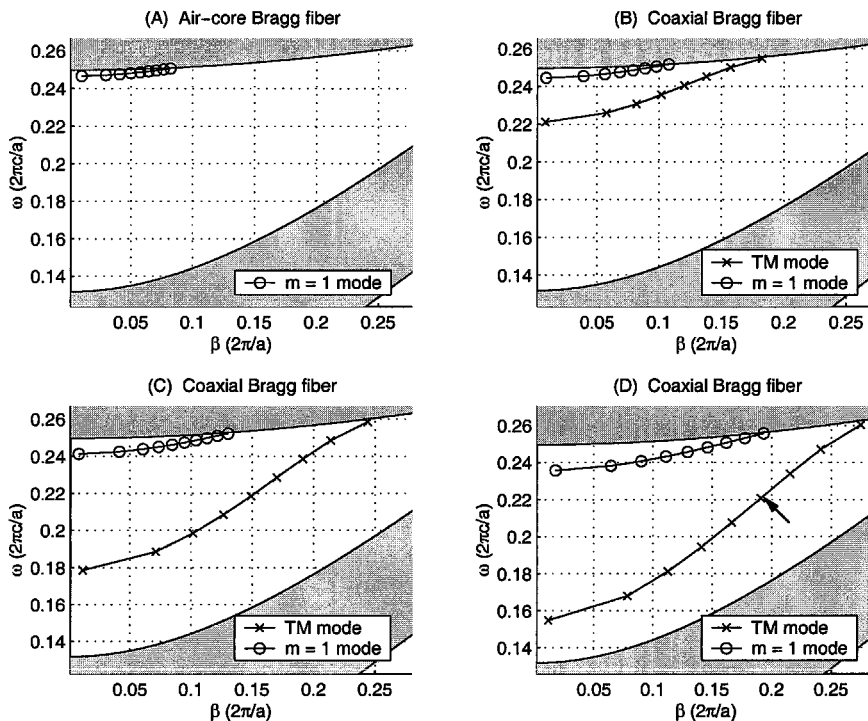


Fig. 6. Dispersion diagrams for $n_i = 4.6$ and $r_o = 0.867a$. $r_i$ is varied as follows: (A) $r_i = 0$ (air-core Bragg fiber), (B) $r_i = 0.133a$, (C) $r_i = 0.2a$, and (D) $r_i = 0.267a$. Note that in (D) the TM mode exhibits single-mode behaviour almost all the way through the bandgap, with the zero-dispersion point (identified by the arrow) falling inside the single-mode frequency range.

## 2.3 FDTD Simulations

Thus far I have used the asymptotic algorithm to study the dispersion properties of the air-core and coaxial Bragg fibers. Now I use 2-D finite difference time domain (FDTD) simulations to verify the validity of the asymptotic approach. The 2-D FDTD algorithm used in this dissertation follows that in [9]. The key observation is that for any mode

propagating in a dielectric structure uniform in the $z$ direction, the $z$ dependence of the fields is simply exp($i\beta z$). For example, one can write the electric field as $\vec{E}(x,y,t)$exp($i\beta z$) and the magnetic field as $\vec{H}(x,y,t)$exp($i\beta z$). As a result, the 3-D Maxwell equations are reduced to an equivalent 2-D form:

$$\left(\nabla_{\perp} + i\beta \vec{e}_z\right) \times \vec{E}(x,y,t) = -\mu_0 \frac{\partial}{\partial t} \vec{H}(x,y,t) \qquad (2\text{-}9)$$

$$\left(\nabla_{\perp} + i\beta \vec{e}_z\right) \times \vec{H}(x,y,t) = \varepsilon(x,y) \frac{\partial}{\partial t} \vec{E}(x,y,t) \qquad (2\text{-}10)$$

where $\nabla_{\perp}$ is defined as $\frac{\partial}{\partial x}\vec{e}_x + \frac{\partial}{\partial y}\vec{e}_y$. One can transform these 2-D differential equations into a set of finite difference equations following the standard finite difference time domain procedure [10]. At the boundaries of the computational domain, perfectly matched layer boundary condition (PML) [11, 12] is used to absorb all the outgoing radiation. For the 2-D FDTD equations and other details about the implementation of the algorithm, the reader should consult [9].

I choose to study the coaxial fiber with reduced $r_o$ whose band diagram is given in Fig. 6(D). Specifically the fiber parameters are given as follows: $n_i = 4.6$, $r_i = 0.267a$, $n_o = 1$, $r_o = 0.867a$, $n_1 = 4.6$, $d_1 = 0.333a$, $n_2 = 1.6$ and $d_2 = 0.667a$, where all the parameters have been defined in Fig. 1. A total of 5 cladding pairs are used, which should provide good mode confinement based on past experiences.

To verify the dispersion curves in Fig. 6(D) with FDTD simulations, I first give the fiber an initial field and let it evolve in time in accordance with the Maxwell's equations, with the value of a chosen field component recorded at each time step. A Fast Fourier Transform (FFT) is then performed on the time evolved data, and according to Fourier theory each confined mode would be represented by a frequency peak in the FFT plot.

Both the asymptotic and the FDTD results are shown in Fig. 7, where the asymptotic curve is simply copied over from Fig. 6(D). One can see that there is a good agreement between the two curves.
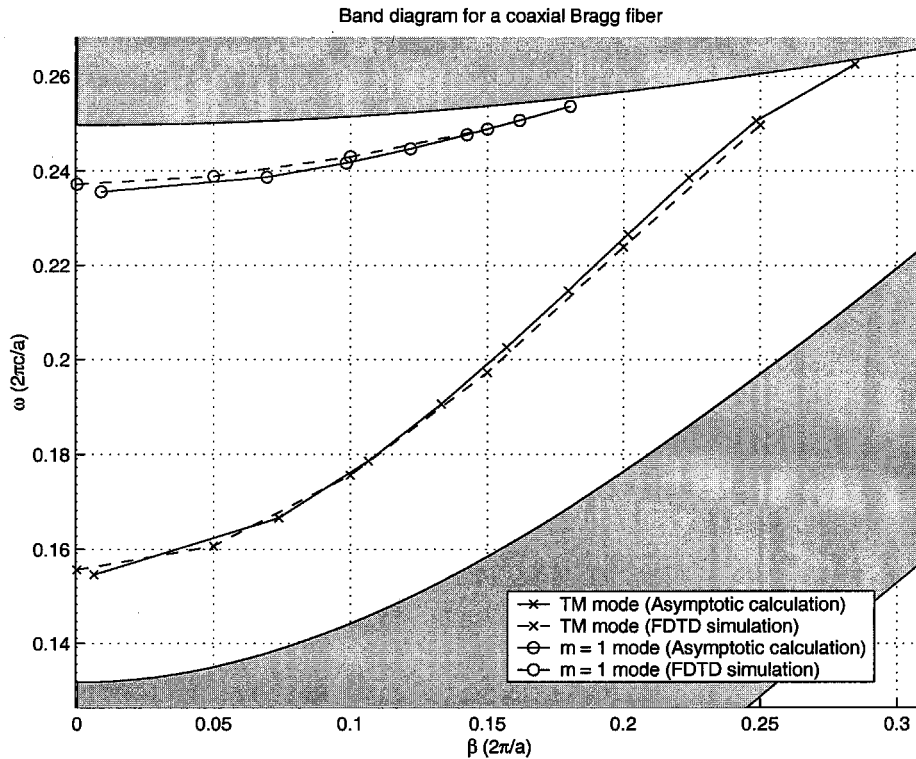


Fig. 7. Asymptotic calculation vs. FDTD simulation. Coaxial fiber band diagram for $n_i =$ 4.6, $r_i = 0.267a$, and $r_o = 0.867a$. The asymptotic curves are copied from Fig. 6(D) and the FDTD structure is defined with 5 cladding pairs.

In Fig. 8, I show the $E_z$ field distribution of a TM mode, filtered out by FDTD simulation. The frequency and propagation constant of the mode are respectively $\omega = 0.2238(2\pi c/a)$ and $\beta = 0.2(2\pi/a)$. Fig. 8 clearly shows that the guided mode has no $\theta$ dependence, just as what one would expect from a TM mode function.
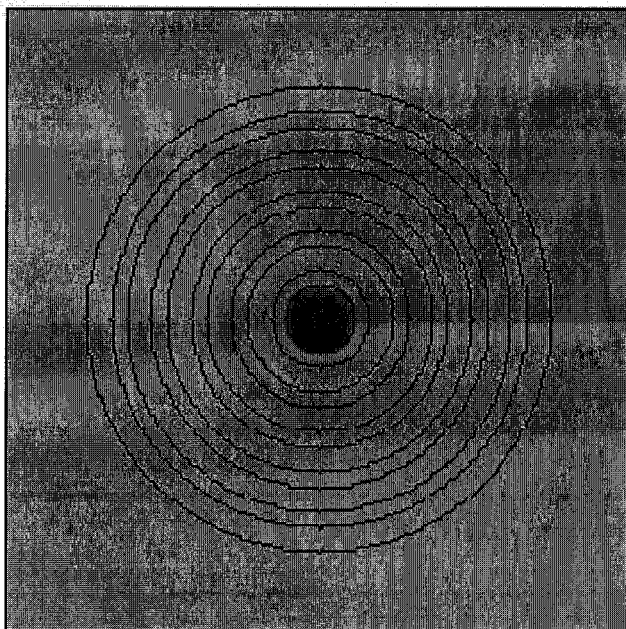
Fig. 8. $E_z$ field distribution of the TM mode. The field is obtained by FDTD calculations. The parameters of the Bragg fiber are given in the caption of Fig. 1 with $n_i$ = 4.6, $r_i$ = 0.267$a$, and $r_o$ = 0.867$a$. The Bragg cladding consists of 5 cladding pairs and the whole fiber is immersed in air. The frequency and propagation constant of the mode are $\omega$ = 0.2238($2\pi c/a$) and $\beta$ = 0.2($2\pi/a$), respectively.

## 2.4 Conclusion

In this chapter I have studied the dispersion properties of both the air-core and coaxial Bragg fibers. The effect of an inner core on fiber dispersion relation has also been characterized by a perturbation analysis. This analysis leads to the discovery of a large single-mode frequency window for the TM mode in the coaxial fiber, which also contains a zero-dispersion point. The validity of my analysis has been verified by FDTD simulations.

*Chapter 3*

# GROUP VELOCITY DISPERSION COMPENSATION IN BRAGG FIBERS

## 3.1 Introduction

In last chapter I compared the dispersion properties of the air-core Bragg fiber and the coaxial Bragg fiber, with special attention to their potential for single-mode transmission. In this chapter I would like to look at another potential application for Bragg fibers: group velocity dispersion compensation. Since guiding light in air lead to lower absorptions loss and reduced nonlinearity effects, I choose to focus only on air-core Bragg fibers.

For years researchers have proposed various schemes to combat chromatic dispersion using Dispersion Compensating Fibers (DCFs) [13]-[17], with dispersion values D typically ranging up to -1,000 ps/(ns·km). Since none of the above-mentioned schemes guide light in air, they inevitably suffer from absorption loss and nonlinearity effects such as self-phase modulation and four-wave mixing [18]. The degree to which these undesirable effects undermine the performance of the DCFs depends on the particular design. In the following sections I will show that it is theoretically possible to design a Bragg fiber that not only guides light in air, but also produces large negative dispersions ($\sim$ -20,000 ps/(nm·km)).

## 3.2 Theoretical Analysis

Once again I refer to the asymptotic matrix theory developed by Xu et al. [7]. In this theory, an arbitrary number of inner dielectric layers, called the "inner region" (IR), are treated exactly, whereas the outside cladding layers, called the "outer region" (OR), are approximated in the asymptotic limit. Approximate mode equations were also derived by matching the boundary conditions at the interface between the IR and the OR, whose accuracy can be improved arbitrarily by including more and more layers in the IR. For the sake of simplicity I begin my analysis of air-core Bragg fiber by matching boundary conditions at the air core boundary and the accuracy of the results will be improved later.

Consider the generic air-core Braggg fiber given in Fig. 9. The mode dispersion relations depend on all five parameters: $n_1$, $n_2$, $r_{core}$, $r_1$ and $r_2$. In the limit of very large radius, the circular Bragg fiber approaches a planar Bragg stack, whose band diagrams and mode equations can be found in standard literature [19]. Hence for low-loss transmission it is necessary to have the Bragg fiber modes to fall inside the TE and/or TM bandgap(s) of the corresponding Bragg stack, whichever is applicable.
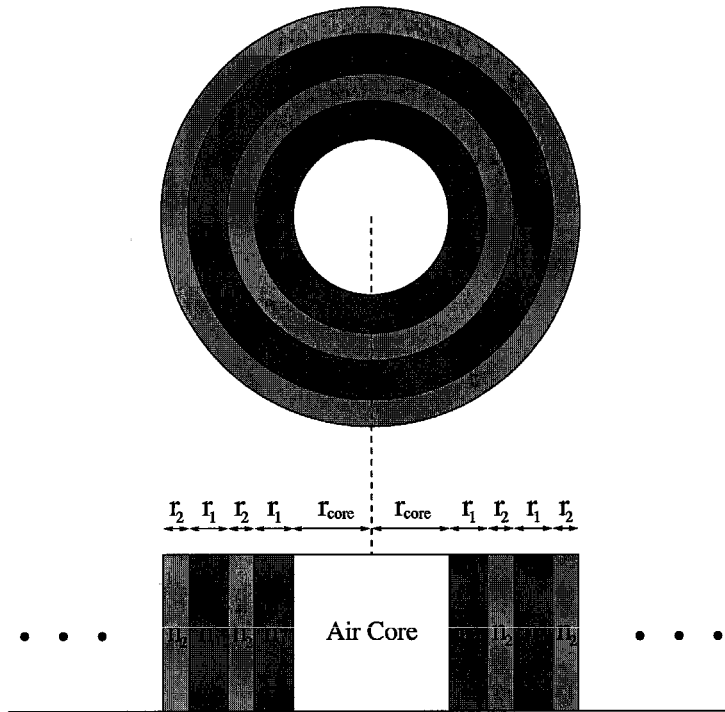


Fig. 9. Schematic of an air-core Bragg fiber. The fiber cladding consists of alternating layers of dielectric media with high and low refractive indices.

Just as in [7] I start with a large index contrast between the cladding layers by setting $n_1 = 4.6$ and $n_2 = 1.5$, so as to result in a large bandgap. The rest of the fiber parameters, $\{r_{core}, r_1, r_2\}$ are found by exhaustive search until I find a single-mode frequency window in which only $m = 1$ modes with negative dispersion exist, where $m$ is the azimuthal index. Note in general modes in a cylindrically symmetric waveguide are designated by two mode numbers, one radial and one azimuthal. In this chapter I discuss only modes with the lowest

radial mode number – all higher-order modes have been "pushed" out of the bandgap by continually shrinking the fiber air core.

The fiber modes can also be classified by their polarization characteristics: the modes are purely TE or TM for $m = 0$, but for $m \neq 0$ they are either TE-like or TM-like (just like the EH and HE modes in conventional fibers). It turns out that the TM and the TM-like modes with the lowest radial number are the last ones to remain in the bandgap as I shrink the core radius. For this reason only these modes and the TM band structure (of the corresponding Bragg stack) are plotted in Fig. 10.
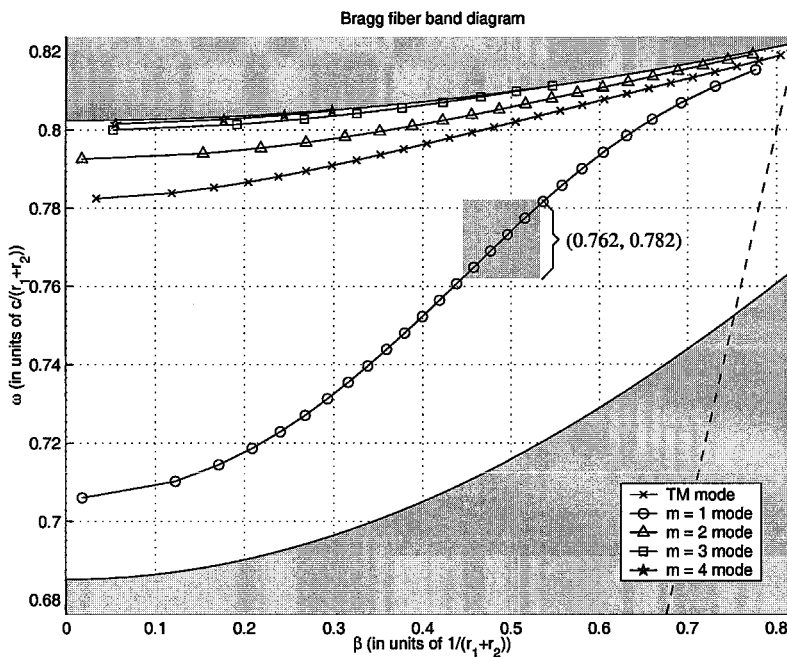


Fig. 10. Dispersion diagram based on asymptotic calculations. Only the TM and TM-like modes with the lowest radial number are plotted, as all other modes have been "pushed" out of the bandgap. The TM band structure of the corresponding Bragg stack serves as the background and the dotted line shown is the light line. Boundary conditions are matched at the air core boundary. The following fiber parameters are used: $n_1 = 4.6$, $n_2 = 1.5$, $r_1 = 10$, $r_2 = 2$, and $r_{core} = 30$, all in normalized units. Note in the frequency window (0.762, 0.782) the $m = 1$ band not only exhibits single-mode behavior but also possesses negative dispersion values.

In Fig. 10 we see that in the frequency window (0.705, 0.782) only the $m = 1$ mode is present and forms a band in the fundamental bandgap. The segment of the band with negative curvature or dispersion (i.e. $d^2\omega/d\beta^2 < 0$) is enclosed in the shaded box spanning the frequency range (0.762, 0.782). Since both the angular frequency $\omega$ and the propagation wave vector $\beta$ have both been normalized in Fig. 10, they need to be "denormalized" before one can compare results with previous works. For instance, if I pick the normalized operating frequency to be $0.77(c/(r_1+r_2))$, which, when converted to 1.55$\mu$m in MKS units, gives a dispersion value D of roughly -25,000 ps/(nm·km), a 25-fold improvement over the previous results. See Fig. 11 for a plot of the dispersion value D in the vicinity of the operating wavelength.
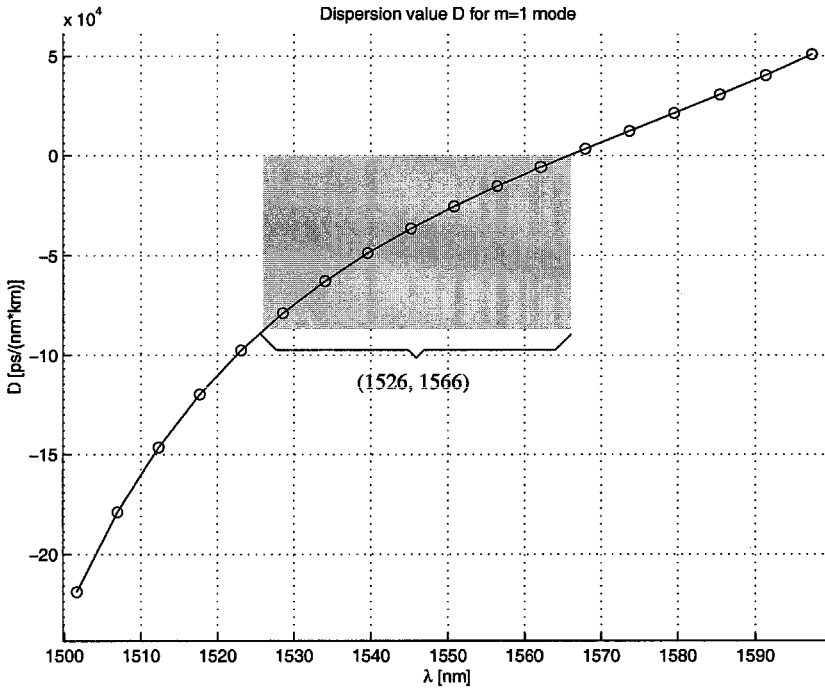


Fig. 11. Dispersion value D for the $m = 1$ band. Curve is plotted based on asymptotic calculations. The second derivative $\partial^2\beta/\partial\omega^2$ is calculated by a direct differential method (i.e., no curve fitting). Fiber structure and boundary matching surface follow those of Fig. 10. Shaded area (1526, 1566) is made to match the frequency window (0.762, 0.782), also in Fig. 10, by choosing the normalized operating frequency to be $0.77(c/(r_1 + r_2))$, which translates to 1.55$\mu$m in MKS units. Note at $\lambda = 1.55\mu$m, dispersion value D $\approx$ −25, 000ps/(nm·km).

## 3.3 Simulation Results

In last section I used the asymptotic algorithm to study the dispersion properties of the air-core Bragg fiber. Now I would like use finite FDTD simulations to verify the validity of my asymptotic calculations.

Following the same approach given in chapter 2 I consider the same Bragg fiber used in last section: $r_{core} = 30$, $n_1 = 4.6$, $r_1 = 10$, $n_2 = 1.5$ and $r_2 = 2$, where the parameters have been defined in Fig. 9. Twelve cladding pairs are used in my simulations to reduce the radiation loss to approximately 0.2dB/km [7].

Both the asymptotic and the FDTD results are shown in Fig. 12, where the asymptotic curve is simply copied over from Fig. 10. I find a good agreement between the two curves.
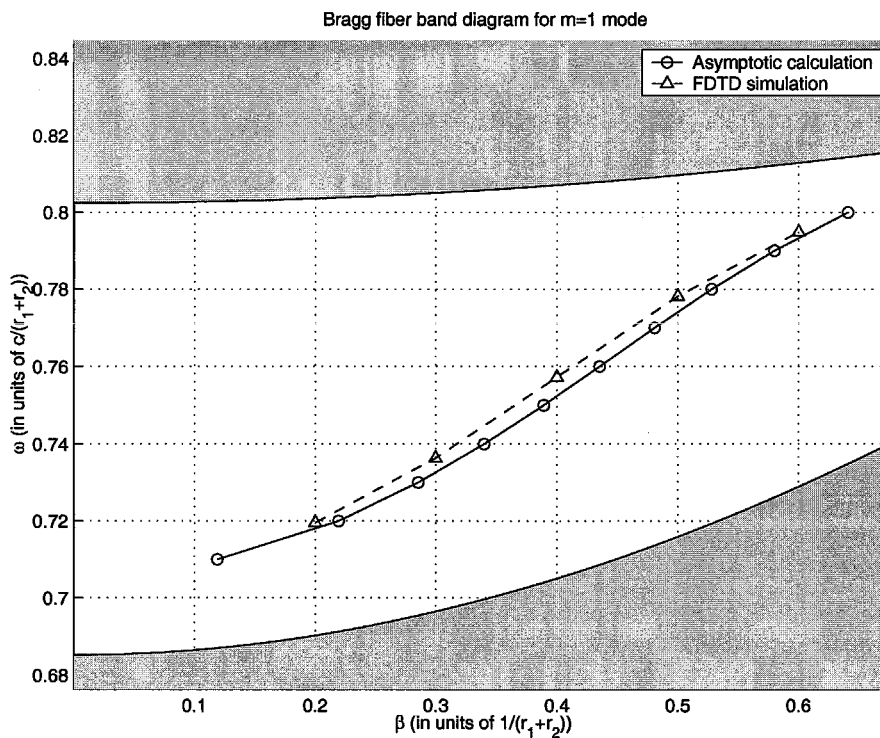


Fig. 12. Dispersion diagram for the $m = 1$ mode. The asymptotic curve is copied from Fig. 10 and the FDTD structure is defined with 12 cladding pairs.

In Fig. 13 I show the distribution of the $H_z$ field obtained from FDTD calculations. The frequency and propagation constant of the mode are respectively $\omega = 0.777(c/(r_1+r_2))$ and $\beta = 0.5(1/(r_1 + r_2))$. Fig. 13 clearly shows that the guided mode has a radial number $l = 0$ (no null in the radial direction inside the core), an azimuthal number $m = 1$ and a significant portion of the field concentrated within the air core.
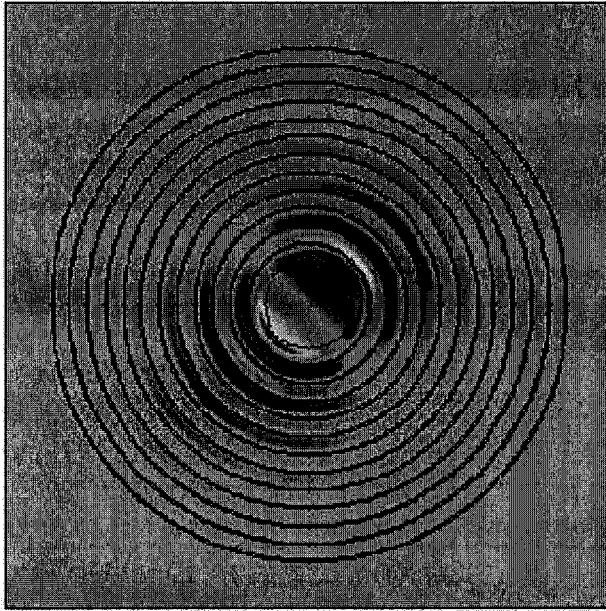


Fig. 13. $H_z$ field distribution of the $m = 1$ mode. The field is obtained by FDTD calculations. The parameters of the Bragg fiber are given in the caption of Fig. 10. The Bragg cladding consists of 12 cladding pairs and the whole fiber is immersed in air. The angular frequency and propagation constant of this mode are $\omega = 0.777(c/(r_1 + r_2))$ and $\beta = 0.5(1/(r_1 + r_2))$, respectively.

## 3.4 Observations and Comments

In Sec. 3.2 I found a frequency window in which only the $m = 1$ mode can propagate. This claim was made, however, based on asymptotic calculations that matched the boundary conditions at the air core boundary (i.e., only one layer in the IR). Would the claim still hold true as I include more layers in the IR, which, as [7] shows, would improve the accuracy of the solutions? The answer is an unfortunate 'No': given sufficient number of cladding layers I have found numerous higher-order cladding modes in the above-

mentioned single-mode frequency window. One such higher-order mode is plotted in Fig. 14, which is found by matching the boundary conditions at the outer surface of the 50th layer (i.e., the IR contains 50 layers). This $m = 4$ band cuts through the frequency window (0.762,0.782), rendering it multi-mode. The $m = 1$ curve is also redrawn under this new boundary matching condition and it does not change much from Fig. 10. In fact my calculations show that as I move the boundary-matching surface from the air core boundary to the 50th cladding layer, the $m = 1$ band converges very quickly from the band in Fig. 10 to the one in Fig. 14. Moving the boundary-matching surface further out into the cladding region would be unnecessary as it would result in only a minimal correction to Fig. 14. Thus I can regard the $m = 1$ band in Fig. 14 as the exact mode solutions and work out the "exact" dispersion value D at the same frequency of $0.77(c/(r_1 + r_2))$, which turns out to be roughly -20,000 ps/(nm·km).
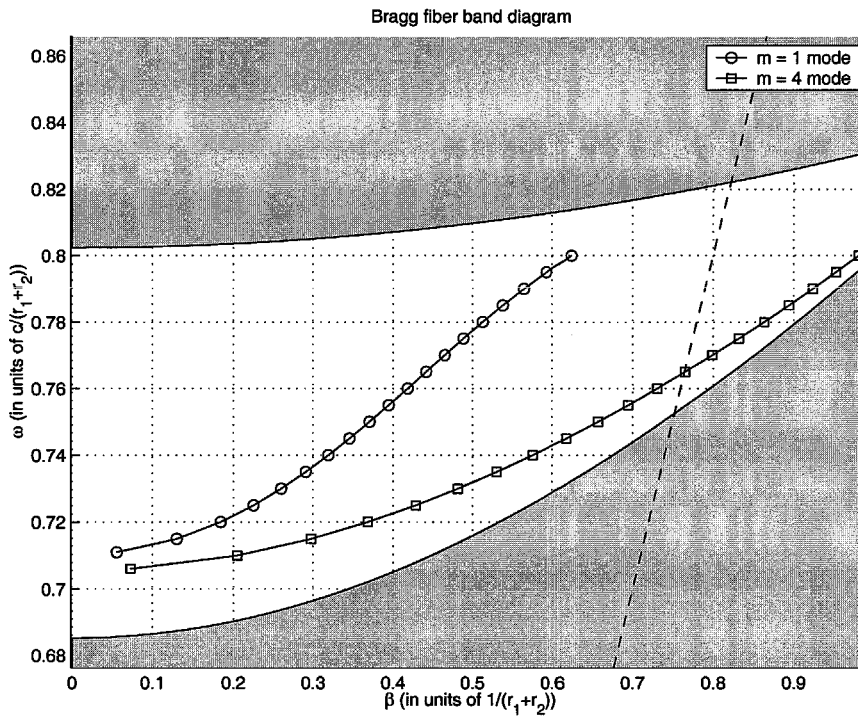


Fig. 14. Dispersion diagram based on asymptotic calculations. Just as in Fig. 10, only the TM-like bands with the lowest radial number are plotted. Boundary conditions are matched at the 50th cladding layer. Fiber parameters are given in the caption of Fig. 10. Note that the $m = 4$ band was missing in Fig. 10.

Just as a side note, the $m = 4$ band in Fig. 14 is not the same as the one in Fig. 10. In fact, as one moves the boundary-matching surface from the air core boundary to the 50th cladding layer, the $m = 4$ mode in Fig. 10 gradually moves up in frequency and eventually disappears from the bandgap. In other words, its presence in Fig. 10 is merely a result of numerical errors inherent in the asymptotic calculations.

Single-mode transmission would seem to be unrealizable if not for the following considerations:

(1) Just like the cladding modes in conventional fibers, the higher-order cladding modes in Bragg fibers also have a much more spread-out field profile than the $m = 1$ modes, which translates into higher loss for fibers with fixed number of cladding layers. This is also manifested in the fact that our first round of asymptotic calculations (by matching boundary conditions at the air core boundary) failed to detect any of the higher-order modes, due to large computation errors incurred by the asymptotic approximations. Theoretically this means one can classify the Bragg fiber modes into two categories based on their confinement characteristics: those of truly confined air-core modes and those of less confined cladding modes. In [7] Xu et al. pointed out that Bragg fibers are not true Bragg structures due to their lack of translational periodicity. Rather, one can view them as Bragg structures with distributed perturbations, with the amount of perturbation decaying to zero as r→∞. Since the asymptotic calculations assume true Bragg confinement after the boundary-matching surface, then any modes that can be detected by matching the boundary conditions at the air core boundary is confined by true Bragg reflections, whereas all the other modes require at least some distributed perturbations to achieve confinement.

A more precise comparison is made in Fig. 15, in which the field profiles of both the $m = 1$ and $m = 4$ modes are plotted at the operating frequency. It is obvious from the plot that the $m = 1$ mode is much more confined that the higher-order mode.
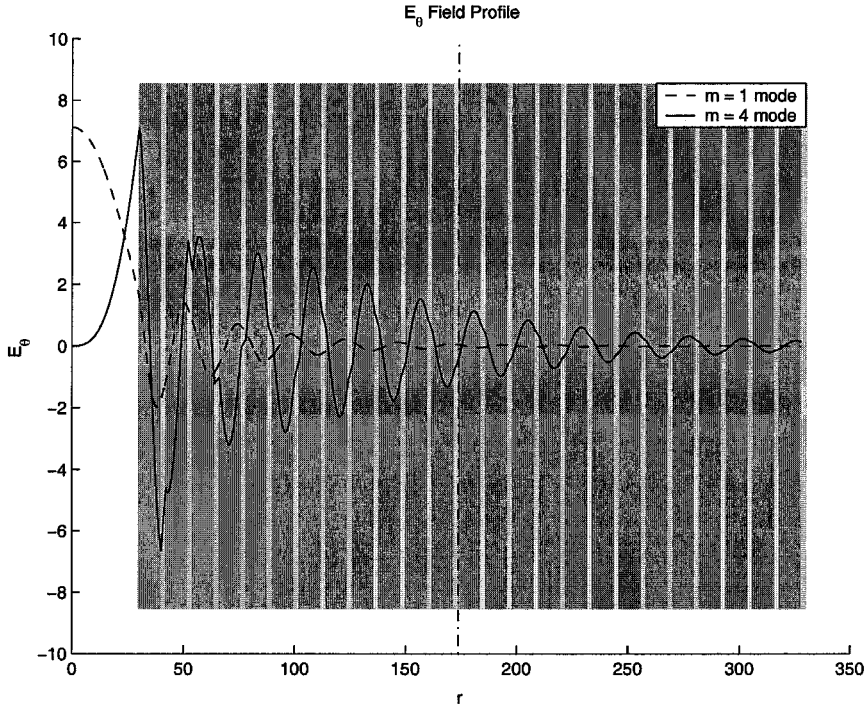
Fig. 15. The radial profile of the $E_\theta$ field. The white area is the fiber core and the shaded layers represent the cladding layers. All fiber parameters are given in the caption of Fig. 10. The vertical dashed line shows the boundary of a fiber structure with 12 cladding pairs, used in the FDTD simulations in Sec. 3.3. The frequency of the mode is $\omega = 0.77(c/(r_1+r_2))$, the chosen normalized operating frequency.

(2) Modes of different azimuthal symmetries are orthogonal. If the incoming fiber is properly aligned with the Bragg DCF, then the incident $m = 1$ mode would theoretically only excite the $m = 1$ mode in the Bragg fiber. Of course in practice fiber misalignment and material imperfections would never allow excitation of $m = 1$ mode alone in the DCF, but I believe it could still be a contributing factor that one can take advantage of.

In my FDTD simulations in Sec. 3.3, no higher-order cladding modes have ever been detected. This is probably due both to large radiation losses and to selective mode excitation by the initial field, consistent with my two arguments above. My speculation is further bolstered by the fact that given enough cladding layers and a proper initial field,

higher-order modes like the $m = 4$ mode in Fig. 14 can indeed be found using FDTD simulations and the results agree well with that given by the asymptotic approach.

I would to stress that this work represents only a theoretical study of the dispersion properties of Bragg fibers and does not represent a design of a realistic DCF. In this report my only aim is to show that it is possible to achieve large negative dispersion through Bragg reflections in Bragg fibers. The choice of large index contrast in the cladding layers is a mere convenience. It not only affords me a large bandgap to work with, but through tight mode confinement also allows the verification of my asymptotic calculations within a reasonable time frame using FDTD simulations. In fact my calculations show that the large negative dispersion value obtained is a direct consequence of Bragg reflection and its order of magnitude does not depend on the index contrast. Also note the material dispersion is deliberately left out of my calculations and simulations, as it depends on the particular choice of materials.

## 3.5 Future Work

Can one fabricate a realistic dispersion-compensating Bragg fiber as it is? The answer is "No". Though Bragg fibers with large index contrast have in fact been made [2], with the high-index layer made of Tellurium ($n = 4.6$), such a high-index material suffers from an absorption loss that is generally several orders of magnitude higher than that of glass, hence making them unusable in long-haul communication systems. Besides, the structural parameters of the Bragg fiber used in this study are not compatible with the those used in the real world. For example, if the normalized frequency of $0.77(c/(r_1 + r_2))$ is converted to the operating wavelength $\lambda = 1.55\mu$m, then the fiber core radius $r_{core}$ works out to be roughly $0.47\mu$m (with $r_1 = 0.16\mu$m, and $r_2 = 0.032\mu$m respectively), which is one order of magnitude smaller than that of a conventional fiber core, hence a huge splicing loss would result. We can probably get around these problems by reducing the index contrast between the cladding layers. The problem, however, is that Bragg fibers of low index contrast require a large number of cladding layers for mode confinement. For example, Bragg fibers with an index contrast of 0.1 in the cladding layers require about 1,000 cladding pairs to

achieve 0.2 dB/km loss [7], which poses a serious problem to fiber manufacturers. Research on reducing the number of cladding layers required for low-index fibers would be the subject of a future paper.

As a final remark, I would like to point out that in this study I have only concerned myself with the dispersion value D, and ignored the other important figure of merit for dispersion compensation, namely, the dispersion slope. This is so because (1) I believe that in a realistic Bragg DCF with low index contrast, the single-mode bandwidth would be so small (due to a very narrow bandgap) that multi-channel compensation is unlikely. (2) there is actually a frequency at which the dispersion D "bottoms out", i.e., dispersion slope is zero at this point. For the Bragg fiber in Fig. 10, this zero-slope point is located well above the the single-mode window, and hence is not shown in Fig. 11. Luckily, I have observed a sizable downward shift in its frequency as I reduce the index contrast, which should work in our favour when one develops the DCF with low index contrast. Once again, the details will be published in a future paper.

*Chapter 4*

## DISCRETE BRAGG GRATING IN PLANAR WAVEGUIDES

### 4.1 Introduction

The analysis in previous chapters focuses on Bragg fibers, where photon confinement in the transverse direction is achieved by Bragg reflections. In this chapter I would like to switch gears and examine Bragg reflections in waveguides of a different geometry. Specifically I would like to study discrete Bragg gratings in planar waveguides, where the Bragg reflections occur along the longitudinal dimension and provide a reflection response suitable for a optical filter.

Optical filter design based on nearly-uniform Fiber Bragg gratings (FBGs) has recently attract much attention as it provides convenient, cost-effective, and reliable solutions to some of the important problems in the high bit-rate wavelength-division multiplexed systems [20]-[24]. All of the schemes proposed so far, however, involve continuous 1-D gratings in optical fibers. It would be interesting to see how one can carry over the solution into waveguides of other geometries, e.g., is it possible to realize the same grating functionalities in a planar waveguide? In particular, given the recent progress in light confinement in 2-D photonic crystal slab waveguides [25]-[26], I would like to take the next logic step and explore the possibility of etching a discrete, nearly-periodic grating in such a structure.

### 4.2 Layer Peeling Algorithm

An 1-D FBG is characterized by the evolution of its effective refractive index $n(z)$ along its length:

$$n(z) = n_0 + \Delta n(z)\cos(K_0 z + \theta(z)) \tag{4-1}$$

where $n_0$ is the average effective refractive index and $K_0(=2\pi/\Lambda)$, $\Delta n(z)$, and $\theta(z)$ specify the grating parameters: $\Lambda$ is the reference period, $\Delta n(z)$ accounts for the local grating strength (apodization), and $\theta(z)$ determines its phase variation and local period.

Various schemes have been proposed to design FBG's that can accommodate almost any filter responses, among them is a so-called "layer-peeling" algorithm, an efficient inverse-scattering algorithm first proposed by Feced et al. [27]. The basic idea is to first discretize the fiber medium into many differential layers and each layer is then approximated by an instantaneous scattering matrix sandwiched between two propagation matrices:

$$M_T \approx M_P M_S M_P \tag{4-2}$$

where $M_T$ is the transfer matrix of the entire layer, $M_s$ is the instantaneous scattering matrix at the center plane of the layer, and $M_p$ is the propagation matrix of each half layer (see Fig. 16). The grating $n(z)$ is then constructed through a recursive procedure based on the target impulse response and the $M_T$ of each layer [27].
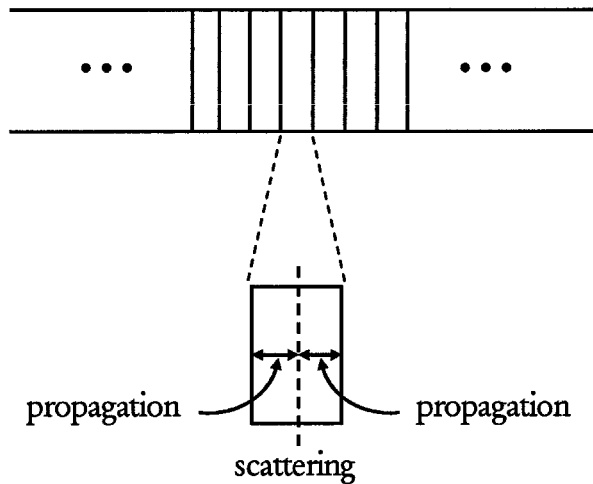


Fig. 16. Layer peeling algorithm. As proposed in [27], the fiber is divided into discrete layers of constant coupling coefficients. The transfer matrix of each layer is then approximated by an instantaneous scattering matrix sandwiched between two identical propagation matrices

## 4.3 Discrete Grating Design

The discretization procedure outlined in the previous section gives us a clue as to how to realize the same grating functionalities in a waveguide with planar geometry. For instance, suppose one implements the instantaneous scattering matrices as a series of discrete air holes, distributed nearly uniformly along the center of a planar waveguide, then the $M_P$ matrices would naturally represent light propagation between adjacent air holes (see Fig. 17).
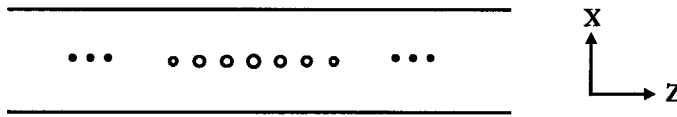


Fig. 17. Top view of a 3-D planar waveguide (the y-dimension is not shown). A seris of air holes (with spacing $\sim \Lambda$) drilled at the center of the waveguide serve as the perturbation. Note that even though I have plotted here a conventional, index-confined rectangular waveguide, the analysis in this chapter can also be extended to more exotic structures such as the multilayer Bragg waveguide or the 2-D photonic crystal slab waveguide.

The refractive index profile should then be rewritten as:

$$\widetilde{n}(x,y,z) = \widetilde{n}_0 + \Delta\widetilde{n}(x,y,z) \qquad (4\text{-}3)$$

where I have used the tilde $\sim$ to differentiate the discrete grating from its continuous counterpart. $\widetilde{n}_0$ now represents the effective refractive index of the unperturbed waveguide (i.e., without the air holes) and $\Delta\widetilde{n}(x,y,z)$ denotes the perturbation (i.e., the air holes).

Provided the air holes are small, one can approximate their perturbative effect by the $\delta$ function weighted by the areas of the individual air holes. Mathematically this means we can expand $\Delta\widetilde{n}(x,y,z)$ in the following form:

$$\Delta\widetilde{n}(x,y,z) = \delta(x)W(y)\sum_m a_m \delta(z - m\Lambda + b_m) \qquad (4\text{-}4)$$

where

$$a_m = \text{(area of the mth air hole)} \times (1 - n_{substrate})$$

$$b_m = \text{deviation of the mth air hole from } z = m\Lambda$$

$$W(y) = 1, \quad \text{if } \frac{-t}{2} < y < \frac{t}{2} \quad \text{("t" is the thickness of the planar waveguide)}$$

$$= 0, \quad \text{otherwise}$$

i.e., $W(y)$ is a windowing function that is nonzero only within the thickness of the waveguide. Embedded in (4-3) and (4-4) is the implicit assumption that the areas of the air holes, hence the $a_m$'s, are small, for otherwise one would not be able to approximate the index perturbation by $\delta$ functions. Additionally the deviation of the air holes from their respective reference locations, i.e., the $b_m$'s, are also taken to be small since the grating is assumed to be "nearly uniform".

Comparing the functional forms of $n(z)$ in (4-1) and $\tilde{n}(x, y, z)$ in (4-3) and (4-4) I arrive at the following intuition:

$$\text{Size of the mth air hole at } z \approx m\Lambda \propto \Delta n(m\Lambda) \tag{4-5}$$

$$\text{Local period of the air holes} \propto \frac{2\pi}{K_0 + \theta'(z)} \tag{4-6}$$

To show that $n(z)$ and $\tilde{n}(x, y, z)$ give the same filter response one needs to go back to the original wave equation. Assuming linearly polarized electric field, say $\vec{E} = E_x$, the perturbed wave equation can be written [28]:

$$\nabla^2 E_x - \mu\varepsilon(\vec{r})\frac{\partial^2 E_x}{\partial t^2} = \mu\frac{\partial^2}{\partial t^2}\left[P_{pert}(\vec{r}, t)\right] \tag{4-7}$$

where $P_{pert}(\vec{r}, t) \propto \Delta(n^2)$ is the electric polarization due to the perturbation. Since $P_{pert}(\vec{r}, t)$ is the only term in the wave equation that provides coupling between the forward

and backward propagating waves, $n(z)$ and $\tilde{n}(x, y, z)$ are equivalent as long as they give equivalent perturbative coupling $P_{pert}(\vec{r}, t)$ .

For the 1-D continuous grating, assuming $\Delta n(z) << n_0$, $P_{pert}(\vec{r}, t)$ is given by (4-1):

$$P_{pert} \propto \Delta(n^2) \approx 2n_0 \Delta n(z) \cos(K_0 z + \theta(z)) \tag{4-8}$$

For sufficiently slowly-varying $\Delta n(z)$ and $\theta(z)$, $\Delta(n^2)$ consists of two distinct Fourier components centered respectively at $\pm K_0$:
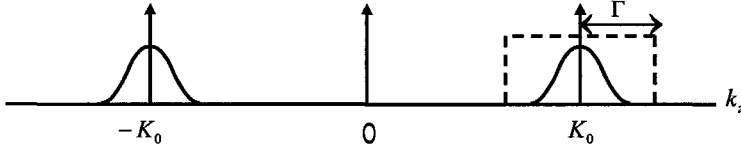


Fig. 18. Fourier spectrum of $\Delta(n^2)$. Valid when $\Delta n(z)$ and $\theta(z)$ are slowly varying.

Without loss of generality I filter out the positive frequency component and apply the sampling theorem on its slowly-varying envelope (including the phase factor $e^{i\theta(z)}$). The end result is an alternative but utterly equivalent expression for the perturbative component at $+K_0$:

$$\Delta(n^2)_{+K_0} = \frac{n_0}{\pi} \left[ \sum_m \Delta n(m\Lambda) e^{i\theta(m\Lambda)} \frac{\sin[(z - m\Lambda)\Gamma]}{z - m\Lambda} \right] e^{iK_0 z} \tag{4-9}$$

where $\Lambda$ is the sampling period and $\Gamma$ is one half of the bandwidth of $\Delta(n^2)_{+K_0}$ (see Fig. 18).

For the case of a discrete grating, I can once again assume $\Delta\tilde{n}(x, y, z) << \tilde{n}_0$ and from (4-3) and (4-4) I find:

$$P_{pert} \propto \Delta(\tilde{n}^2) \approx 2\tilde{n}_0 \Delta \tilde{n}(x, y, z) = 2\tilde{n}_0 \delta(x) W(y) \sum_m a_m \delta(z - m\Lambda + b_m) \qquad (4\text{-}10)$$

Ignoring $\delta(x)$ and $W(y)$ for now and once again assuming $a_m$'s and $b_m$'s are sufficiently slowly-varying, I plot the Fourier spectrum of $\Delta(\tilde{n}^2)$:
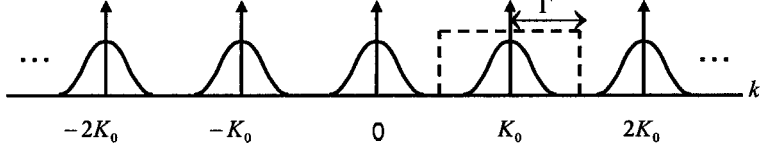


Fig. 19. Fourier spectrum of $\Delta(\tilde{n}^2)$. Valid when $a_m$'s and $b_m$'s are slowly varying. Note only the two resonant components at $K_0$ and $-K_0$ can provide coupling between the forward and backward propagating waves.

Note only the two components located at $K_0$ and $-K_0$ can provide coupling between the forward and backward propagating waves and hence are relevant in my analysis. Once again I filter out the component at $+K_0$ with a pass-band bandwidth of $2\Gamma$:

$$\Delta(\tilde{n}^2)_{+K_0} = \frac{2\tilde{n}_0}{\pi} \left[ \sum_m a_m e^{ib_m K_0} \frac{\sin[(z - m\Lambda + b_m)\Gamma]}{z - m\Lambda + b_m} \right] e^{iK_0 z} \qquad (4\text{-}11)$$

Equating $\Delta(n^2)_{+K_0}$ with $\Delta(\tilde{n}^2)_{+K_0}$ and assuming $b_m$'s are small, one obtains the following relations:

$$a_m = \frac{n_0}{2\tilde{n}_0} \Delta n(m\Lambda) \qquad (4\text{-}12)$$

$$b_m = \frac{\theta(m\Lambda)}{K_0} \qquad (4\text{-}13)$$

Since $a_m$ is proportional to the area of the $m$th air hole, (4-12) confirms my first intuition in (4-5).

What about the second intuition in (4-6)? First of all one needs to define what "local period" means. In Fig. 20 I plot a few air holes in the vicinity of the *m*th air hole.
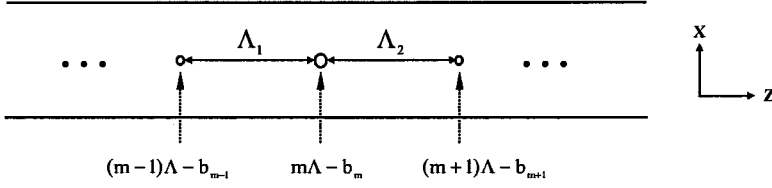


Fig. 20. Local period at the *m*th air hole. The local period at a given air hole is defined to be the average of the distances to the two adjacent air holes, i.e., $(\Lambda_1 + \Lambda_2)/2$ .

If one defines the local period at the *m*th air hole as the average of $\Lambda_1$ and $\Lambda_2$, and recalls that $K_0 = 2\pi/\Lambda$, one gets:

$$
\begin{aligned}
\text{Local period at the mth air hole} &= \frac{\Lambda_1 + \Lambda_2}{2} \\
&= \frac{2\Lambda - b_{m+1} + b_{m-1}}{2} \\
&= \Lambda\left[1 - \frac{\theta[(m+1)\Lambda] - \theta[(m-1)\Lambda]}{4\pi}\right] \\
&\approx \Lambda\left[1 - \frac{2\Lambda\theta'(m\Lambda)}{4\pi}\right] \\
&= \frac{2\pi}{K_0}\left[1 - \frac{\theta'}{K_0}\right] \\
&\approx \frac{2\pi}{K_0 + \theta'}
\end{aligned}
\tag{4-14}
$$

where I have substituted in (4-13) for $b_{m+1}$ and $b_{m-1}$ and made the slowly-varying assumption on $\theta(z)$. (4-14) indeed confirms my second intuition in (4-6).

One last thing that needs to be addressed is the $\delta(x)$ and $W(y)$ functions that I have deliberately left out of $\Delta(\tilde{n}^2)$ in my derivation so far. I shall show in the following that the

inclusion of the two functions requires the introduction of an extra scaling factor $\gamma$ into $\Delta \tilde{n}(x, y, z)$, i.e.,

$$\tilde{n}(x, y, z) = \tilde{n}_0 + \Delta \tilde{n}(x, y, z) = \tilde{n}_0 + \gamma \delta(x) W(y) \sum_m a_m \delta(z - m\Lambda + b_m) \tag{4-15}$$

where $\gamma$ is presumably highly dependent on the geometry of the waveguide.

$\gamma$ can be computed by matching scattering equations. In Appendix B I derive the scattering equations for wave propagation in FBR's (i.e., the continuous grating), and so long as the goal is to generate the same filter response via a discrete grating in a planar waveguide, one needs to reproduce the same set of scattering equations in the new waveguide as well. Following through the derivation in Appendix B, I realize that, in making the continuous to discrete transition, the following substitution needs to be made:

$$\Delta(n^2)_{continuous} = 2n_0 \Delta n(z) \cos(K_0 z + \theta(z)) \Rightarrow \Delta(\tilde{n}^2)_{discrete} = \gamma \delta(x) W(y) \left[2n_0 \Delta n(z) \cos(K_0 z + \theta(z))\right]$$

where I have applied equality between (4-8), (4-9) and (4-11). Then for the planar waveguide, equation (B-11) becomes:

$$\frac{e^{-i\omega t}}{2} \left[ b_B E_B K_0 \beta e^{-i\frac{K_0 z}{2}} + b_F E_F K_0 \beta e^{i\frac{K_0 z}{2}} - iK_0 b_B' E_B e^{-i\frac{K_0 z}{2}} + iK_0 b_F' E_F e^{i\frac{K_0 z}{2}} \right]$$

$$= \mu \frac{\partial^2}{\partial t^2} \left\{ \gamma \delta(x) W(y) n_0 \varepsilon_0 \Delta n(z) \cos(K_0 z + \theta(z)) \left[ \left( b_B E_B e^{-i\frac{K_0 z}{2}} e^{-i\omega t} + b_F E_F e^{i\frac{K_0 z}{2}} e^{-i\omega t} \right) \right] \right\} \tag{4-16}$$

For the sake of discussion I consider a TE wave (i.e., $\vec{E} = E_x$), the orthonormality relation is given by [28]:

$$\iint E_m E_n^* dx dy = \frac{2\omega\mu}{k_m} \delta_{mn} \tag{4-17}$$

where the integral is taken over the entire transverse plane and $k_m$ is the propagation constant of the $m$th mode.

As in Appendix B I can replace the $\frac{\partial^2}{\partial t^2}$ operator in (4-16) by $-\omega^2$, multiply both sides by $E_B^*(x,y) = E_F^*(x,y)$, integrate over the entire transverse plane, and then apply the orthonormality relation (4-17). Collecting resonant terms in the resultant equation such as the ones that vary as $e^{iK_0 z}$ and comparing them with (B-12), which is the target scattering equation I am hoping to reproduce, I find the following equality relation needs to be satisfied:

$$\frac{2\omega\mu}{k_m} = \gamma \int_{-t}^{+t} |E_m(0,y)|^2 dy \tag{4-18}$$

where $t$ is the thickness of the planar waveguide and $E_m = E_B = E_F$. Or in other words,

$$\gamma = \frac{2\omega\mu}{k_m \int_{-t}^{+t} |E_m(0,y)|^2 dy} \approx \frac{2\omega_0\mu}{\frac{K_0}{2} \int_{-t}^{+t} |E_m(0,y)|^2 dy} = \frac{2\mu c}{\tilde{n}_0 \int_{-t}^{+t} |E_m(0,y)|^2 dy} \tag{4-19}$$

where I have approximated $\omega$ by $\omega_0$, the center frequency, and $k_m$ by $K_0/2$. $c$ is the speed of light in vacuum and $\tilde{n}_0$ is the effective modal index given by (4-3).

## 4.4 Conclusion

I present in this chapter an efficient scheme for designing discrete and nearly-uniform Bragg gratings in planar waveguides, which in principle are capable of performing any functionalities that can be achieved by continuous FBG's. One limitation of my design, which I did not explore in this theoretical study, is the potentially significant scattering losses that could be associated with the air holes. More theoretical and experimental work is needed on this subject.

BIBLIOGRAPHY

[1] P. Yeh, A. Yariv, and E. Marom, "Theory of Bragg fiber," J. Opt. Soc. Amer. 68, 1196-1201 (1978).

[2] Y. Fink, D. J. Ripin, S. Fan, C. Chen, J. D. Joannopoulos, and E. L. Thomas, "Guiding optical light in air using an all-dielectric structure," J. Lightwave Technol. 17, 2039-2041 (1999).

[3] M. Miyagi, A. Hongo, Y. Aizawa, and S. Kawakami, "Fabrication of germanium-coated nickel hollow waveguides for infrared transmission," Appl. Phys. Lett. 43, 430-432 (1983).

[4] N. Croitoru, J. Dror, and I. Gannot, "Characterization of hollow fibers for the transmission of infrared radiation," Appl. Opt. 29, 1805-1809 (1990).

[5] R. F. Cregan, B. J. Mangan, J. C. Knight, T. A. Birks, P. St. J. Russell, P. J. Roberts, and D. C. Allan, "Single-mode photonic band gap guidance of light in air," Science 285, 1537-1539 (1999).

[6] M. Ibanescu, Y. Fink, S. Fan, E. L. Thomas, J. D. Joannopoulos, "An all-dielectric coaxial waveguide," Science 289, 415-419 (2000).

[7] Y. Xu, G. Ouyang, R. Lee, and A. Yariv, "Asymptotic matrix theory of Bragg fibers," J. Lightwave Technol. 20, 428-440 (2002).

[8] Roy J. Glauber and M. Lewenstein, "Quantum optics of dielectric media," Phy. Rev. A 43, 467-491 (1991).

[9] F. Zepparelli, P. Mezzanotte, F. Alimenti, L. Roselli, R. Sorrentino, G. Tartarini, and P. Bassi, "Rigorous analysis of 3D optical and optoelectronic devices by the compact-2D-FDTD method." Opt. and Quantum Electron. 31, 827-841 (1999).

[10] K. S. Yee, "Numerical solution of initial boundary value problems involving Maxwell's equations in isotropic media," IEEE Trans. Antennas Propag. AP-14, 302-307 (1966).

[11] J. P. Berenger, "A perfectly matched layer for the absorption of electromagnetic waves," J. Computat. Phys. 114, 185-200 (1994).

[12] S. D. Gedney, "An anisotropic perfectly matched layer-absorbing medium for the truncation of FDTD lattices," IEEE Trans. Antennas Propag. 44, 1630-1639 (1996).

[13] A. Vengsarkar and W. A. Reed, "Dispersion-compensating single-mode fibers: efficient designs for first- and second-order compensation," Opt. Lett. 18, 924-926, (1993).

[14] A. Bjarklev, T. Rasmussen, O. Lumholt, K. Rottwitt, and M. Helmer, "Optimal design of single-cladded dispersion-compensating optical fibers," Opt. Lett. 19, 457-459, (1994).

[15] B. Jopson and A. Gnauck, "Dispersion compensation for optical fiber systems," IEEE Comm. Mag. 33, 96-102, (1995).

[16] Onishi M, Kashiwada T, Ishiguro Y, Nishimura M, and Kanamori H, "High-performance dispersion-compensating fibers," Fiber Integ. Opt. 16, 277-285, (1997).

[17] C. Bradford, "Managing chromatic dispersion increases bandwidth," Laser Focus World, February (2001).

[18] M.R.C. Caputo and M.E. Gouvea, "Dispersion slope effects of the compensation dispersion fiber for broadband dispersion compensation in the presence of self-phase modulation," Laser Focus World, February (2001).

[19] P. Yeh, A. Yariv, and C. Hong, "Electromagnetic propagation in periodic stratified media. I. General theory," J. Opt. Soc. Am. 67, 423-438, (1977).

[20] J. Zhang, P. Shum, S. Y. Li, et al., "Design and fabrication of flat-band long-period grating," IEEE Photonics Technol. Lett. 15, 1558-1560, (2003).

[21] J. Skaar and O. H. Waagaard, "Design and characterization of finite-length fiber gratings," IEEE J. Quantum Elect. 39, 1238-1245, (2003).

[22] H. P. Li, Y. L. Sheng, Y. Li, et al. "Phased-only sampled fiber Bragg gratings for high-channel-count chromatic dispersion compensation," J. Lightwave Technol. 21, 2074–2083, (2003).

[23] L. G. Sheu, K. P. Chuang, and Y.C. Lai, "Fiber bragg grating dispersion compensator by single-period overlap-step-scan exposure," IEEE Photonics Technol. Lett. 15, 939-941, (2003).

[24] M. Ibsen and R. Feced, "Fiber Bragg gratings for pure dispersion-slope compensation," Opt. Lett. 28, 980-982, (2003).

[25] A. Yariv, "Coupled-wave formalism for optical waveguiding by transverse Bragg reflection," Opt. Lett. 27, 936-938, (2002).

[26] W. Kuang and J.D. O'Brien, "Reducing the out-of-plane radiation loss of photonic crystal waveguides on high-index substrates," Opt. Lett. 29, 860-862, (2004).

[27] R. Feced, M. N. Zervas, and M. A. Muriel, "An efficient inverse scattering algorithm for the design of nonuniform fiber Bragg gratings", IEEE J. Quantum Elect. 35, 1105-1115, (1999).

[28] A. Yariv and P. Yeh, "Optical waves in crystals", John Wiley and Sons, (1984).

**Appendix A: Field Calculations inside the Bragg Fiber Core**

In this appendix I would like to derive the analytic expressions for various transverse $\vec{E}$ field components inside the inner core region of the Bragg fiber. The resulting expressions and their physical interpretations are used in the perturbation analysis in Chapter 2.

If I take the $z$ axis as the direction of propagation, then every field component in the fiber takes the following form:

$$\psi(r,\theta,z,t) = \phi(r,\theta)e^{i(\beta z - \omega t)} \tag{A-1}$$

where $\psi$ can be $E_z$, $E_r$, $E_\theta$, $H_z$, $H_r$, or $H_\theta$. $\omega$ is the angular frequency and $\beta$ is the propagation constant.

From waveguide theory we know that the transverse field components can be expressed in terms of $E_z$ and $H_z$. In particular, $E_r$ and $E_\theta$ can be written as [1]:

$$E_r = \frac{i\beta}{\omega^2\mu\varepsilon - \beta^2}\left(\frac{\partial}{\partial r}E_z + \frac{\omega\mu}{\beta}\frac{\partial}{r\partial\theta}H_z\right) \tag{A-2}$$

$$E_\theta = \frac{i\beta}{\omega^2\mu\varepsilon - \beta^2}\left(\frac{\partial}{r\partial\theta}E_z - \frac{\omega\mu}{\beta}\frac{\partial}{\partial r}H_z\right) \tag{A-3}$$

Inside the core,

TM mode:  $E_r$ is the only transverse $\vec{E}$ field component, and

$$E_z = AJ_0(k_{co}r) \tag{A-4}$$

where $k_{co}$ is the transverse wavevector inside the core,

$$k_{co} = \sqrt{\frac{n^2\omega^2}{c^2} - \beta^2} \tag{A-5}$$

Using (A-2) the $E_r$ component can be written:

$$E_r = \frac{i\beta}{\frac{n^2\omega^2}{c^2} - \beta^2}\left(\frac{\partial}{\partial r}E_z\right)$$

$$= \frac{i\beta}{\frac{n^2\omega^2}{c^2} - \beta^2}\frac{d}{dr}\left[AJ_0(k_{co}r)\right]$$

$$= \frac{i\beta k_{co}A}{\frac{n^2\omega^2}{c^2} - \beta^2}J_0'(k_{co}r) \tag{A-6}$$

$$= \frac{-i\beta k_{co}A}{\frac{n^2\omega^2}{c^2} - \beta^2}J_1(k_{co}r)$$

$l = 1$ mode:  both $E_r$ and $E_\theta$ are present in the core, and

$$E_z = AJ_1(k_{co}r)\cos\theta \tag{A-7}$$

$$H_z = CJ_1(k_{co}r)\sin\theta \tag{A-8}$$

$$E_r = \frac{i\beta}{\frac{n^2\omega^2}{c^2} - \beta^2}\left(\frac{\partial}{\partial r}E_z + \frac{\omega\mu}{\beta}\frac{\partial}{r\partial\theta}H_z\right)$$

$$= \frac{i\beta}{\frac{n^2\omega^2}{c^2} - \beta^2}\left\{\frac{\partial}{\partial r}\left[AJ_1(k_{co}r)\cos\theta\right] + \frac{\omega\mu}{r\beta}\frac{\partial}{\partial\theta}\left[CJ_1(k_{co}r)\sin\theta\right]\right\}$$

$$= \frac{i\beta\cos\theta}{\frac{n^2\omega^2}{c^2} - \beta^2}\left\{Ak_{co}J_1'(k_{co}r) + \frac{\omega\mu C}{r\beta}J_1(k_{co}r)\right\} \tag{A-9}$$

$$= \frac{i\beta\cos\theta}{\frac{n^2\omega^2}{c^2} - \beta^2}\left\{Ak_{co}J_0(k_{co}r) + \left(\frac{\omega\mu C}{r\beta} - \frac{Ak_{co}}{k_{co}r}\right)J_1(k_{co}r)\right\}$$

$$= \frac{i\beta\cos\theta}{\frac{n^2\omega^2}{c^2} - \beta^2}\left\{A + \frac{\omega\mu C}{\beta}\right\}\frac{k_{co}}{2} \quad as \ r \to 0,$$

where to go from the third equality to the fourth equality I have made use of the identity $J_1'(k_{co}r) = J_0(k_{co}r) - \frac{1}{k_{co}r}J_1(k_{co}r)$. And to reach the last equality I

have used the fact that as $r \to 0$, $J_0(k_{co}r) \to 1$ and $J_1(k_{co}r) \to \frac{k_{co}r}{2}$ . By the same token,

$$
\begin{aligned}
E_\theta &= \frac{i\beta}{\frac{n^2\omega^2}{c^2} - \beta^2} \left( \frac{\partial}{r\partial\theta} E_z - \frac{\omega\mu}{\beta} \frac{\partial}{\partial r} H_z \right) \\
&= \frac{-i\beta\sin\theta}{\frac{n^2\omega^2}{c^2} - \beta^2} \left\{ \frac{A}{r} J_1(k_{co}r) + \frac{\omega\mu C}{\beta} \frac{\partial}{\partial r} [J_1(k_{co}r)] \right\} \\
&= \frac{-i\beta\sin\theta}{\frac{n^2\omega^2}{c^2} - \beta^2} \left\{ \frac{A}{r} J_1(k_{co}r) + \frac{\omega\mu k_{co} C}{\beta} \left[ J_0(k_{co}r) - \frac{1}{k_{co}r} J_1(k_{co}r) \right] \right\} \quad \text{(A-10)} \\
&= \frac{-i\beta\sin\theta}{\frac{n^2\omega^2}{c^2} - \beta^2} \left\{ \frac{\omega\mu k_{co} C}{\beta} J_0(k_{co}r) + \left( \frac{A}{r} - \frac{\omega\mu k_{co} C}{\beta k_{co}r} \right) J_1(k_{co}r) \right\} \\
&= \frac{-i\beta\sin\theta}{\frac{n^2\omega^2}{c^2} - \beta^2} \left\{ A + \frac{\omega\mu C}{\beta} \right\} \frac{k_{co}}{2} \quad as \; r \to 0.
\end{aligned}
$$

**Appendix B: Scattering Equations in Fiber Bragg Gratings**

In this appendix I derive the scattering equations for wave propagation in Fiber Bragg Gratings (FBG's). The scattering equations provide a mathematical description for the coupling between two counter-propagating waves in the fiber: $b_B(z,\beta)$ (backward propagating) and $b_F(z,\beta)$ (forward propagating) [27]

$$\frac{db_B(z,\beta)}{dz} + i\beta b_B(z,\beta) = q(z)b_F(z,\beta) \tag{B-1}$$

$$\frac{db_F(z,\beta)}{dz} - i\beta b_F(z,\beta) = q^*(z)b_B(z,\beta) \tag{B-2}$$

where $\beta$ is the detuning parameter

$$\beta = \frac{2kn_0 - K_0}{2} \tag{B-3}$$

and $k$ is the wavevector in vacuum ($= \omega/c$). $q(z)$ (and its complex conjugate $q^*(z)$) gives the coupling strength and is related to the grating parameters as:

$$q(z) = \frac{iK_0}{2n_0}\frac{\Delta n(z)}{2}e^{-j\theta(z)} \tag{B-4}$$

where $\Delta n(z)$ and $\theta(z)$ have been defined in (4-1).

To simplify the derivation I first assume the electric field is linearly polarized, say $\vec{E} = E_x$, and then expand the total field as:

$$E_x = \frac{1}{2}e^{-i\omega t}\left[b_B(z,\beta)E_B(x,y)e^{-i\frac{K_0 z}{2}} + b_F(z,\beta)E_F(x,y)e^{i\frac{K_0 z}{2}}\right] \tag{B-5}$$

Plug the above expression into the perturbed wave equation

$$\nabla^2 E_x - \mu\varepsilon(\vec{r})\frac{\partial^2 E_x}{\partial t^2} = \mu\frac{\partial^2}{\partial t^2}\left[P_{pert}(\vec{r},t)\right] \tag{B-6}$$

we get

$$\frac{e^{-i\omega t}}{2}\left[b_B\, e^{-i\frac{K_0 z}{2}}(-\frac{K_0^2}{4}E_B + \frac{\partial^2 E_B}{\partial x^2} + \frac{\partial^2 E_B}{\partial y^2} + \omega^2\mu\varepsilon E_B) + \right.$$
$$b_F\, e^{i\frac{K_0 z}{2}}(-\frac{K_0^2}{4}E_F + \frac{\partial^2 E_F}{\partial x^2} + \frac{\partial^2 E_F}{\partial y^2} + \omega^2\mu\varepsilon E_F) -$$
$$\left. iK_0 b'_B E_B\, e^{-i\frac{K_0 z}{2}} + iK_0 b'_F E_F\, e^{i\frac{K_0 z}{2}} \right]$$
$$= \mu\frac{\partial^2}{\partial t^2}P_{pert}(\vec{r},t) \tag{B-7}$$

where prime denotes derivative with respect to $z$. Note in the derivation above I have also made the following slowly-varying assumptions on wave amplitudes $b_B$ and $b_F$:

$$b''_B \ll \frac{K_0}{2}b'_B\,; \qquad b''_F \ll \frac{K_0}{2}b'_F \tag{B-8}$$

So all terms containing $b''_B$ and $b''_F$ have been omitted from (B-7).

From the unperturbed wave equation we know

$$-(kn_0)^2 E_B + \frac{\partial^2 E_B}{\partial x^2} + \frac{\partial^2 E_B}{\partial y^2} + \omega^2\mu\varepsilon E_B = 0 \tag{B-9}$$

where $k = \omega/c$ and $n_0$ is the effective modal refractive index of the unperturbed waveguide. One can then expand $(kn_0)^2$ as

$$(kn_0)^2 = \left(\frac{K_0}{2} + \beta\right)^2 \approx \frac{K_0^2}{4} + K_0\beta \tag{B-10}$$

since $\beta << K_0$. Plugging (B-9) and (B-10) into (B-7), one finds the first term in the square brackets becomes

$$b_B \mathrm{E}_B K_0 \beta \, e^{-i\frac{K_0 z}{2}}$$

Similarly the second term in the square brackets becomes

$$b_F \mathrm{E}_F K_0 \beta \, e^{i\frac{K_0 z}{2}}$$

Put them together, we get

$$\frac{e^{-i\omega t}}{2}\left[ b_B \mathrm{E}_B K_0 \beta \, e^{-i\frac{K_0 z}{2}} + b_F \mathrm{E}_F K_0 \beta \, e^{i\frac{K_0 z}{2}} - iK_0 b'_B \mathrm{E}_B \, e^{-i\frac{K_0 z}{2}} + iK_0 b'_F \mathrm{E}_F \, e^{i\frac{K_0 z}{2}} \right]$$

$$= \mu \frac{\partial^2}{\partial t^2} P_{pert}$$

$$= \mu \frac{\partial^2}{\partial t^2} \left[ \Delta(n^2)\varepsilon_0 E_y \right] \tag{B-11}$$

$$= \mu \frac{\partial^2}{\partial t^2} \left\{ 2n_0 \Delta n(z)\cos(K_0 z + \theta(z))\varepsilon_0 \times \frac{1}{2}\left[ \left( b_B \mathrm{E}_B \, e^{-i\frac{K_0 z}{2}} \, e^{-i\omega t} + b_F \mathrm{E}_F \, e^{i\frac{K_0 z}{2}} \, e^{-i\omega t} \right) \right] \right\}$$

For a lossless fiber we have $\mathrm{E}_B(x, y) = \mathrm{E}_F(x, y)$. So I can cross them out on both sides of (B-11). Also if we replace the $\frac{\partial^2}{\partial t^2}$ operator by $-\omega^2$ and collect the resonant terms, say the ones that vary as $e^{-iK_0 z}$, we get the following equation:

$$b'_B + i\beta b_B = \frac{-i}{n_0 k_0}(\omega^2 \mu \varepsilon_0 n_0^2)\Delta n(z) e^{-i\theta(z)} b_F \tag{B-12}$$

but we also know

$$\omega^2 \mu\varepsilon_0 n_0^2 = \frac{n_0^2 \omega^2}{c^2} = (kn_0)^2 = \left(\frac{K_0}{2} + \beta\right)^2 \approx \frac{K_0^2}{4} \qquad \text{(B-13)}$$

Plugging into (B-12), we have

$$b_B' + i\beta b_B = -\frac{iK_0}{4n_0} \Delta n(z) e^{-i\theta(z)} b_F = q(z)b_F \qquad \text{(B-14)}$$

where $q(z)$ has been defined in (B-4). Thus (B-14) gives back the original scattering equation (B-1). In a similar fashion, by collecting resonant terms with $e^{iK_0 z}$ dependence one could also derive (B-2) from (B-11).